PERGAMON

Journal of Structural Geology 23 (2001) 1883–1899

JOURNAL OF STRUCTURAL GEOLOGY

www.elsevier.com/locate/jstrugeo

Pseudo 3-D modeling of trishear fault-propagation folding

Ernesto O. Cristallini[a,b,*], Richard W. Allmendinger[a]

[a]Department of Earth and Atmospheric Sciences, Cornell University, Ithaca, NY, USA
[b]CONICET — Departamento de Ciencias Geológicas, Universidad de Buenos Aires, Paellon II, 1424 Ciudad de Buenos Aires, Argentina

Received 21 June 2000; revised 1 February 2001; accepted 28 February 2001

Abstract

Basement structures, to which trishear fault-propagation models have most successfully been applied, are commonly three-dimensional folds formed at the tip-line of a fault. We present here a 'pseudo-3D' trishear model in which various parameters are permitted to vary along strike and oblique-slip can be modeled. These variations may be combined in an infinite number of ways, facilitating the simulation of many real structures. A thrust changing from blind to emergent can be produced by a change in the slip or propagation-to-slip (*P*/*S*) along strike. Folds with forelimbs changing from overturned to upright along strike can be modeled either by changing the slip, P/S or trishear angle. Also some minor folds perpendicular or oblique to the main structure can result from changes in the trishear angle or fault angle along the strike. Models including growth strata show that it is practically impossible to distinguish between growth and pre-growth strata using the map patterns. As a field test, we have modeled the oblique slip East Kaibab monocline, demonstrating a good fit between the field observations and model predictions.

Keywords: Trishear fault-propagation folding; Basement structures; East Kaibab monocline; 3-D analysis; Growth strata

1. Introduction

The trishear kinematic model (Erslev, 1991; Erslev and Rogers, 1993; Erslev and Mayborn, 1997) is becoming recognized as a broad, generally applicable model of fault-propagation folding. To date, virtually all work on the model has been in two dimensions (2D), assuming plane strain (Erslev, 1991; Erslev and Rogers, 1993; Erslev and Mayborn, 1997; Hardy and Ford, 1997; Allmendinger, 1998). One of the areas where the concept has been applied most successfully is in the realm of basement-involved 'thick-skinned' structures such as those in the Laramide Rocky Mountain foreland (Erslev, 1991; Erslev and Rogers, 1993; Allmendinger, 1998) or in the Neuquén Basin of Argentina (Allmendinger et al., 2001). These structures are commonly characterized by aspect ratios (strike parallel length to strike normal width) of 3:1 to about 8:1 (Jordan and Allmendinger, 1986), in contrast to the aspect ratio of typical thrust-belt structures that may be 20:1 or greater. The low aspect ratios of thick-skinned deformation in map view leads to the conclusion that fault and fold parameters may change in a short distance along strike, motivating a three-dimensional (3D) approach.

Here we present a pseudo-3D, forward kinematic model of trishear fault-propagation folding, where the deformation is analyzed as serial 2D cross-sections. Although this approach is not truly 3D, volume is nonetheless preserved to within a fraction of a percent. Thus, these results closely mimic a true 3D kinematic model. A variety of complex 3D geometries can be reproduced by along strike variation in slip, trishear angle, propagation-to-slip-ratio (*P*/*S*), and rake of the slip vector. The predictions of the model are compared with recently published data from the East Kaibab monocline of the Colorado Plateau (Tindall and Davis, 1999).

2. Background

The basic concept of a triangular shear zone was first proposed by Eric Erslev (1991) to explain deformation zones associated with Laramide Rocky Mountain basement uplifts. Erslev's initial geometric description of either footwall or hanging wall attached trishear zone was refined by Hardy and Ford's (1997) velocity description and their realization that the propagation to slip ratio (*P*/*S*) could have a large range of values rather than be restricted to either zero (footwall attached) or one (hanging wall

* Corresponding author. Correspondence address: CONICET — Departamento de Ciencias Geológicas, Universidad de Buenos Aires, Paellon II, 1424 Ciudad de Buenos Aires, Argentina. Tel.: +54-11-4576-3329; fax: +54-11-4576-3329.

E-mail address: ernesto@gl.fcen.uba.ar (E.O. Cristallini).

0191-8141/01/$ - see front matter
PII: S0191-8141(01)00034-7

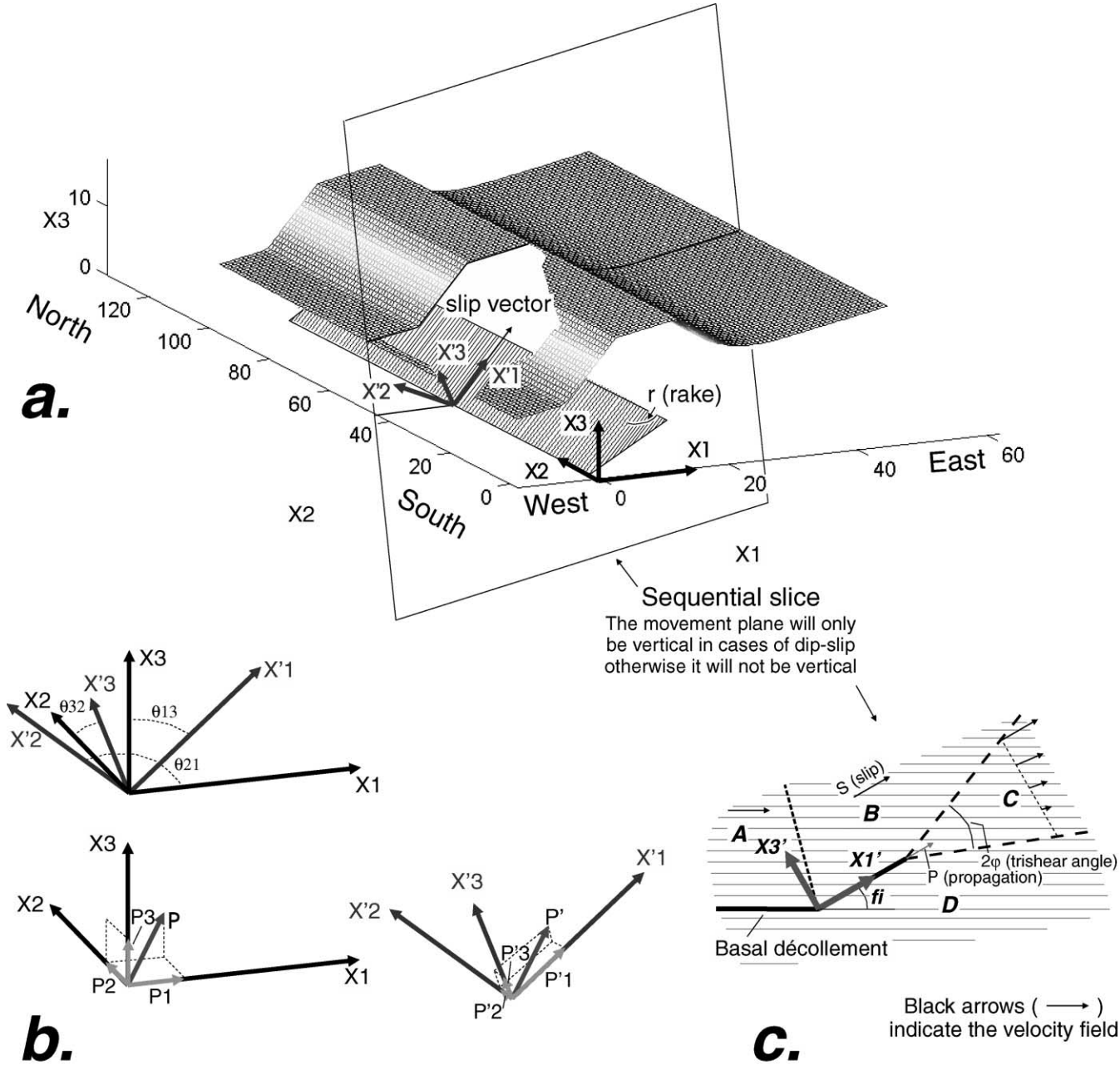

Fig. 1. Parameters and coordinate systems used in 3-D trishear. (a) The 'geographic system' in which X_1 (east) and X_2 (north) are horizontal, and perpendicular and parallel, respectively, to the strike of the fault. X_3 is vertical and positive upward. The 'movement plane' coordinate system: X'_1 is parallel to the slip vector in the plane of the fault, X'_2 is perpendicular to the movement plane and parallel to the fault plane, and X'_3 is the pole to the fault. The rake for an oblique-slip case is indicated. In this and all subsequent figures, different shades of gray indicate different bedding heights; the scales of all the axes are equal and are in arbitrary program units. (b) Angular relations between coordinate systems. (c) Three or four fields of motion (labeled A–D) are defined in the plane of movement (sequential slice), depending on whether the fault ramps up from a basal décollement. A and B are in the hanging wall of the fault, C corresponds to the trishear zone, and D, the footwall of the fault, is stationary. The slip velocity (S) and propagation velocity (P) are indicated as well as the trishear angle (2φ) and the fault angle (f_i) for each serial section.

attached). Allmendinger (1998) presented a numerical grid search for objective determination of trishear parameters in naturally occurring structures, and recently Zehnder and Allmendinger (2000) have presented a precise way of deriving a range of symmetric and asymmetric velocity fields.

Three-dimensional analysis of trishear deformation was initially studied by Cooper and Hardy (1999), Fischer et al. (1999) and Fischer and Wilkerson (2000). These authors link serial sections together as we do here. However, they assume strictly dip-slip displacement, whereas we allow for oblique-slip. The main purpose of Fischer and Wilkerson's

(2000) work was not an investigation of trishear kinematics but an attempt to predict fracture orientations from an analysis of surface curvature. In the future, a 3D extension of the Zehnder and Allmendinger (2000) approach will result in a true 3D analysis.

3. Implementation of pseudo-3D algorithm

If the slip vectors on the fault plane were always assumed to be parallel to the dip and perpendicular to the tip line, the problem of linking serial 2D cross-sections together would be strictly graphical. However, one of the most interesting classes of 3D problems is that which involves oblique-slip. Thus, in this section, we develop the coordinate transformations necessary to analyze oblique-slip deformation after first describing the basics of our computer simulation of pseudo-3D trishear.

3.1. Trishear kinematics in pseudo-3D

The slip vector and the pole to the fault surface define the movement plane of a fault. Moving one rigid block over another on a planar fault will produce a single family of slip vectors in which vectors on all parts of the fault are parallel. This process is inherently one of plane strain: if slip is constant along strike, there is no strain along the null-axis perpendicular to the movement plane. Thus, we define sequential cross-sections, all parallel to the movement plane of the fault. In the models presented here there are generally 100–200 of these sections side-by-side. A larger number of parallel sections would result in a higher resolution model at the expense of additional computation time.

3.1.1. Coordinate transformations for oblique-slip

We define two right-handed coordinate systems: the first is a 'geographic system' in which X_1 (east) and X_2 (north) are horizontal, and perpendicular and parallel, respectively, to the strike of the fault. X_3 is vertical and positive upward (Fig. 1a and b). The movement plane of the fault defines the second coordinate system: X'_1 is parallel to the slip vector in the plane of the fault, X'_2 is perpendicular to the movement plane and parallel to the fault plane, and X'_3 is the pole to the fault, and of course is parallel to the movement plane.

Bedding is defined by a 2D array of up to 200×200 points, depending on the number of serial sections. The actual points that compose the array are calculated from the intersections of an initially horizontal surface with the sequential movement planes. Points are spaced equally along each line of intersection with 200 points in each serial section. During fault movement, the grid points are translated in the X'_1, X'_2, and X'_3 (i.e. fault) coordinate system and then transformed into the X_1, X_2, and X_3 system for plotting and visualization. The transformation matrix, **a**, between the coordinate systems (Fig. 1) is composed of the cosines of the angles between the two sets of axes (Fig. 1):

$$a_{ij} = \begin{pmatrix} a_{11} & a_{12} & a_{13} \\ a_{21} & a_{22} & a_{23} \\ a_{31} & a_{32} & a_{33} \end{pmatrix} = \begin{pmatrix} \cos\theta_{11} & \cos\theta_{12} & \cos\theta_{13} \\ \cos\theta_{21} & \cos\theta_{22} & \cos\theta_{23} \\ \cos\theta_{31} & \cos\theta_{32} & \cos\theta_{33} \end{pmatrix}.$$

Using the geometry of the fault in the coordinate system and the orthogonality relations, all of the components of the transformation matrix can be derived:

$$a_{ij} = \begin{pmatrix} \left(\sqrt{1 - a_{12}^2 - a_{13}^2}\right) & \cos(r) & \cos\left(\pi - \frac{\pi}{2} - M\right) \\ \left(\frac{-a_{22}a_{32} - a_{23}a_{33}}{a_{31}}\right) & \cos\left(r - \frac{\pi}{2}\right) & \left(\frac{a_{22}a_{32}a_{11} - a_{12}a_{22}a_{31}}{a_{31}a_{31} - a_{33}a_{11}}\right) \\ \cos\left(\frac{\pi}{2} + f_i\right) & \cos\frac{\pi}{2} & \cos(f_i) \end{pmatrix}$$

where f_i is the fault angle in each serial section (i), r is the rake angle and M is given by:

$$M = \tan^{-1}\left\{ \frac{\dfrac{\cos r}{\cos[\tan^{-1}(\tan r \cos f_i)]}}{\left[\left(\dfrac{\cos r}{\cos[\tan^{-1}(\tan r \cos f_i)]}\right)^2 + 1\right]^{\frac{1}{2}}} \right\} + 2\tan^{-1}1$$

A point P in the grid with geographic coordinates (P_1, P_2, P_3) will be transformed to the fault coordinate system by (see Fig. 1):

$$P'_1 = a_{11}P_1 + a_{12}P_2 + a_{13}P_3$$
$$P'_2 = (a_{21}P_1 + a_{22}P_2 + a_{23}P_3) - i$$
$$P'_3 = a_{31}P_1 + a_{32}P_2 + a_{33}P_3$$

and the reverse transformation will be:

$$P_1 = a_{11}P'_1 + a_{21}P'_2 + a_{31}P'_3$$
$$P_2 = (a_{12}P'_1 + a_{22}P'_2 + a_{32}P'_3) + i$$
$$P_3 = a_{13}P'_1 + a_{23}P'_2 + a_{33}P'_3$$

where i is the number of the sequential slice.

The total slip specified for the model is applied in incremental steps to each of the sequential slices. If the rake

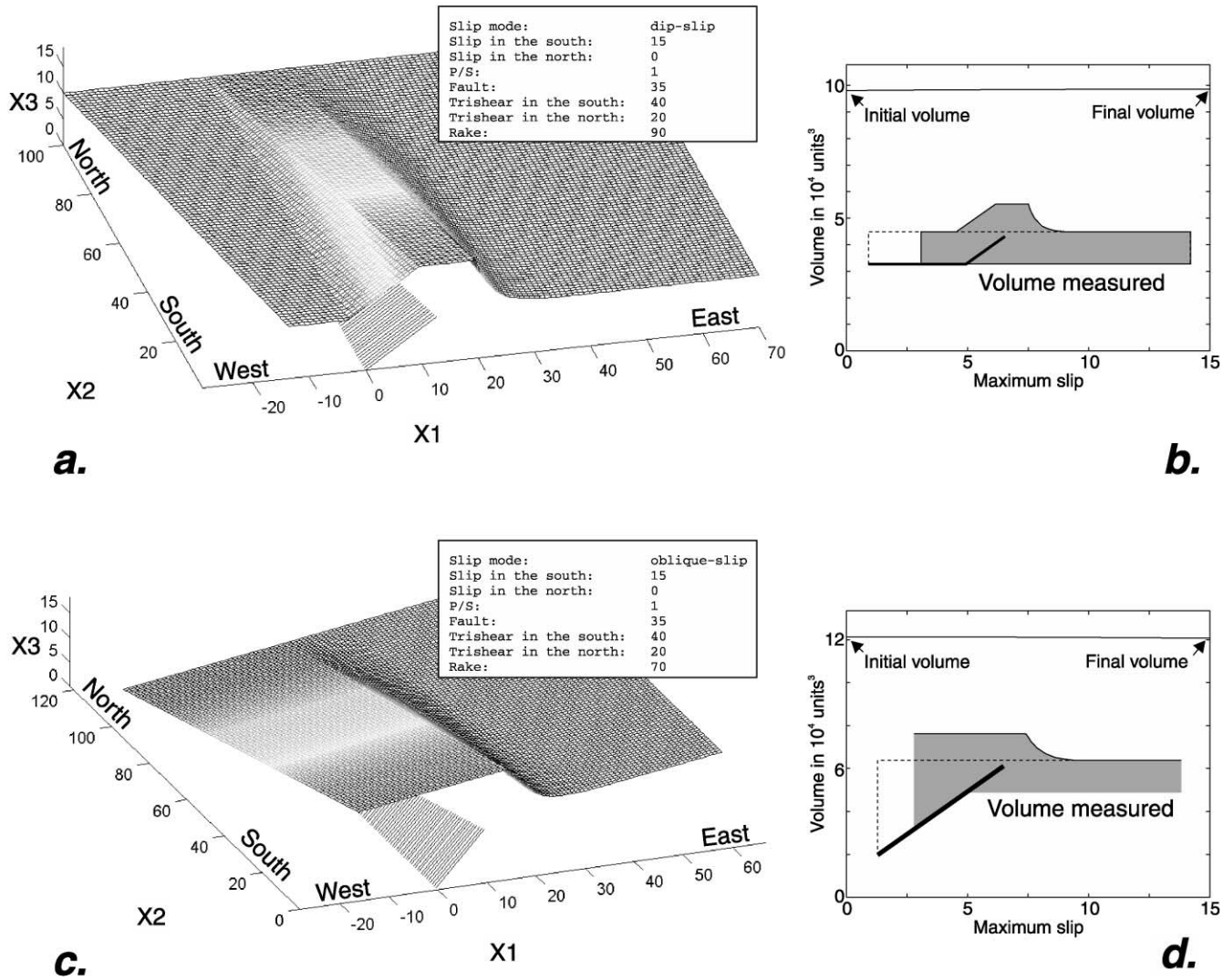

Fig. 2. Demonstration of volume conservation in the pseudo-3D model, for the case of: (a and b) a ramp from a decollement, and (c and d) a fault with no bends. Despite the 3D variations in trishear angle and slip, the changes in volume in the models are $\ll 1\%$. Slip and *P/S* are in arbitrary program units, the fault, trishear and rake angles are in degrees.

is 90°, then the user can specify a step up from a basal décollement because the movement planes for the décollement and the ramp are parallel. For rakes of other than 90°, we only model the ramp. Three or four fields of motion (labeled A–D in Fig. 1c) are defined in the movement plane (X'_1, X'_2, and X'_3 coordinate system), depending on whether or not the fault ramps up from a basal décollement. Fields A and B are in the hanging wall of the fault, C corresponds to the trishear zone, and D is the footwall of the fault. In each step of fault displacement, points are moved at a constant velocity parallel to the fault if they are located in field A or B, or moved according to the velocity description of trishear given by Hardy and Ford (1997) if they are in field C. All points in the footwall (field D) are stationary.

Zehnder and Allmendinger (2000) have demonstrated that there are an infinite number of velocity fields that can be applied within the trishear zone conserving the area of the cross-section. However, the simple linear velocity field (Fig. 1c) has been shown to fit many structures very well (Hardy and Ford, 1997). Of course, in 3D, the number of velocity fields possible to conserve the volume of the model are also infinite, and the pseudo-3D approximation used in this paper is only one of those velocity fields.

3.1.2. The movement plane and preservation of volume

If slip or ramp angle varies along strike, there must be a minute amount of shear between adjacent sections. In such cases the null-axis cannot be parallel to the intermediate principal axis of strain and there must be small strike parallel movement violating the above assumptions. Our first task is to assess how this affects our assumption of volume conservation by measuring the volume beneath a bedding surface at each step of movement (Fig. 2). In Fig. 2 we show that the volume is conserved with less than 1% of error in both dip-slip and oblique-slip cases. This error

depends strongly on the number of sequential slices, grid points used in the model and slip in each stage of movement. However, it is not very sensitive to different rakes, or changes of trishear parameters along strike (slip, *P*/*S*, trishear angle or fault angle).

3.2. Determination of 3D strain

To calculate the 3D strain, we simulate an initial sphere with an array of 961 points. The spheres are distributed uniformly on a grid, across the entire bedding surface (Fig. 3). The position of each point in a sphere is determined relative to the three or four zones described above and the point moved accordingly. The deformed spheres approximate ellipsoids if the strain within the region circumscribed by the points is more or less homogeneous. Where the strain is quite heterogeneous, very irregular ellipsoids can result. The smaller the original sphere, the more regular the resulting ellipsoid, so we generate small initial spheres (diameter of three units) and then amplify them for visualization. The program also calculates, using the least-squares method, the best-fitting true ellipsoids that approximate the points of irregular strain ellipsoid (Fig. 3). Using this method, we calculate the position and values of the three principal axes of the final strain ellipsoids of the model (Fig. 3). This way we can compare numerical models with field data from a structure, such as strained objects or crystals, fault strain analyses, or magnetic susceptibility anisotropy data. At small displacements, the modeled ellipsoid approximates the infinitesimal strain ellipsoid, enabling a comparison with 3D fracture analysis such as that proposed by Reches (1978).

4. Forward modeling of 3D geometries

Any or all the trishear variables can vary along the strike of a modeled structure, either linearly or by specifying an arbitrary function. That is, we can change the initial position of the tip line, the slip, the fault ramp angle, the trishear apical angle, the propagation-to-slip ratio (*P*/*S*) and also the symmetry of the trishear zone along the strike. In addition, any rake of the slip vector on the fault plane can be specified. With this procedure, we can construct many fold-termination geometries and fold-shape changes along strike. Below, we examine each variable separately to understand its influence on 3D-fold shape, beginning with dip-slip examples.

4.1. Variable slip

The variation in the slip along strike of the fault produces fold terminations that simulate the noses of real structures (Fig. 4a). Because we use parallel kink-style fault-bend folding to model the backlimb, that part of the fold nose has a boxy shape. The forelimb part of the fold nose is smoothly curving because it was modeled using trishear (Fig. 4a and b). The variations in the apparent thickness of the forelimb beds in a map view (Fig. 4b) is due to the inherent changes in thickness predicted by the trishear model (Erslev, 1991) and the variations in the dip of the beds. Note that the width of the anticlinal crest increases at higher stratigraphic levels but is constant along strike for any particular stratigraphic horizon. The crest width is defined by the backlimb, hanging wall-fixed kink axis and the initial position of the hanging wall trishear boundary, for $P/S \geq 1.0$. For $P/S < 1.0$, material that was initially part of the undeformed crest migrates into the trishear zone with time, thus narrowing the crest with time.

The resulting strain ellipsoids within the trishear zone (Fig. 4a) are prolate with the maximum principal axis (S_1) inclined toward the backlimb and a minimum principal axis (S_3) that dips toward the forelimb. The intermediate axis is sub-horizontal with $S \approx 1$. This model produces a slight counter-clockwise rotation, which is to be expected given the northward loss of displacement.

4.2. Variable P/S

The *P*/*S* exerts a fundamental control on fold geometry. By applying *P*/*S* variations along the strike, we can produce folds that evolve from a gently-dipping to a steep-dipping or overturned forelimb, and from a blind thrust to an emergent fault due to the change in tip line position along strike (Fig.4c and d). In map view (Fig. 4d), a change in the apparent thickness of the beds of the forelimb results in a divergence of the bed traces in the direction of diminishing *P*/*S*. The narrowing of the crest northward along strike is due, in part, to $P/S < 1.0$ in the north. The resulting strain ellipsoids (Fig. 4c) are similar to those found for the case of slip variations. However, because this model has constant slip, the amount of rotation (clockwise in this case) is insignificant.

4.3. Variable trishear apical angle

A decrease in the trishear apical angle along the strike results in progressive steepening of the forelimb (Fig. 5a and b). This case is similar to the previous example of P/S variation; however, here the tip line position along strike does not change and thus the fault does not change from blind to emergent along strike. The resulting strain ellipsoids (Fig. 5a) are similar to the ones displayed earlier. The small difference in rotation between the two cases results from adjacent points in different sequential cross-sections with different trishear angles being subjected to slightly different velocity fields.

Striking 3D structures can be produced where the trishear angle first increases and then decreases along strike (Fig. 5c and d). As the trishear apical angle increases, the forelimb broadens markedly and shallows in dip. The result is a small fold which trends perpendicular to the main structure in dip-slip cases or oblique in oblique-slip examples. The reduction in forelimb dip in the middle of the main structure produces a scoop-shaped cut-out in the crest of the fold but the backlimb is unaffected. Because the mechanical

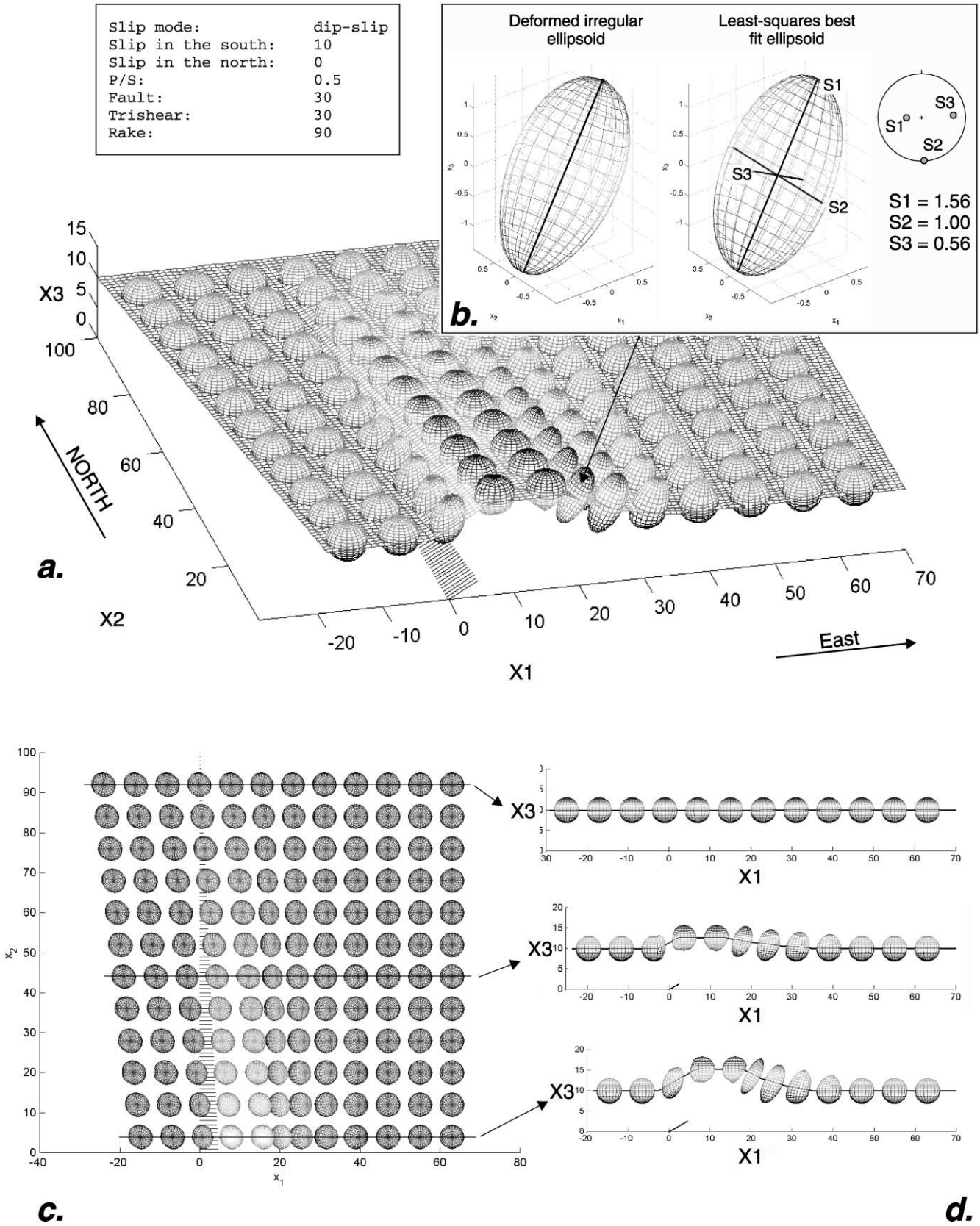

Fig. 3. Calculation of 3D strain using an array of 961 points that, initially, describe a sphere. Spheres are distributed on a grid uniformly across the entire bedding surface. Upon deformation, the array approximates an ellipsoid if the strain within the region circumscribed by the points is more or less homogeneous. The smaller the original sphere, the more nearly homogeneous the resulting ellipsoid; those shown here are amplified for visualization. (a) 3D view. (b) The program calculates a least-squares best-fit ellipsoid that approximates the points of the irregular strain ellipsoid, yielding the position and values of the three principal axes of finite strain. (c) Map view of the model of (a). (d) Three cross-sections through the structure, see location in (c).

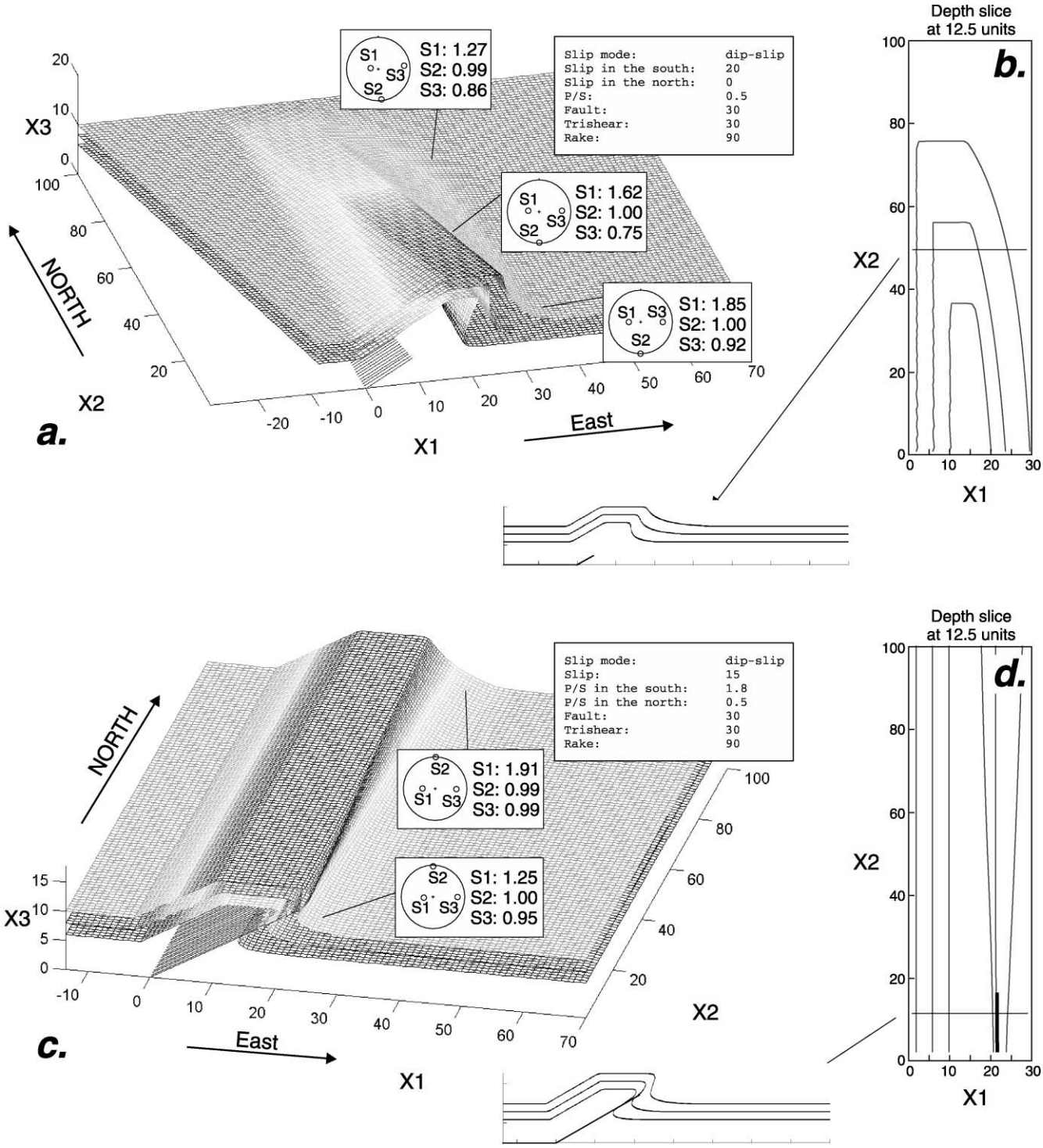

Fig. 4. (a) Fold geometry resulting from a variation in slip along strike. The initial thickness of all the beds is the same. (b) Depth-slice of model in (a) at 12.5 units. A cross-section through the model is shown. Boxy shape of the nose is due to fault-bend fold kinematics used for the backlimb. The forelimb curved nose results from trishear kinematics. (c) Fold geometry due to *P*/*S* variation along strike. The initial thickness of all the beds is the same. (d) Depth-slice of model in (c) at 12.5 units. A cross-section through the model is shown. Fault is emergent in the south (heavy line between 0–20), but blind farther north. Fold is overturned in the south but upright in the north. In map view, a change in the apparent thickness of the beds of the forelimb results in a divergence of the bed traces toward the area with a lower *P*/*S*.

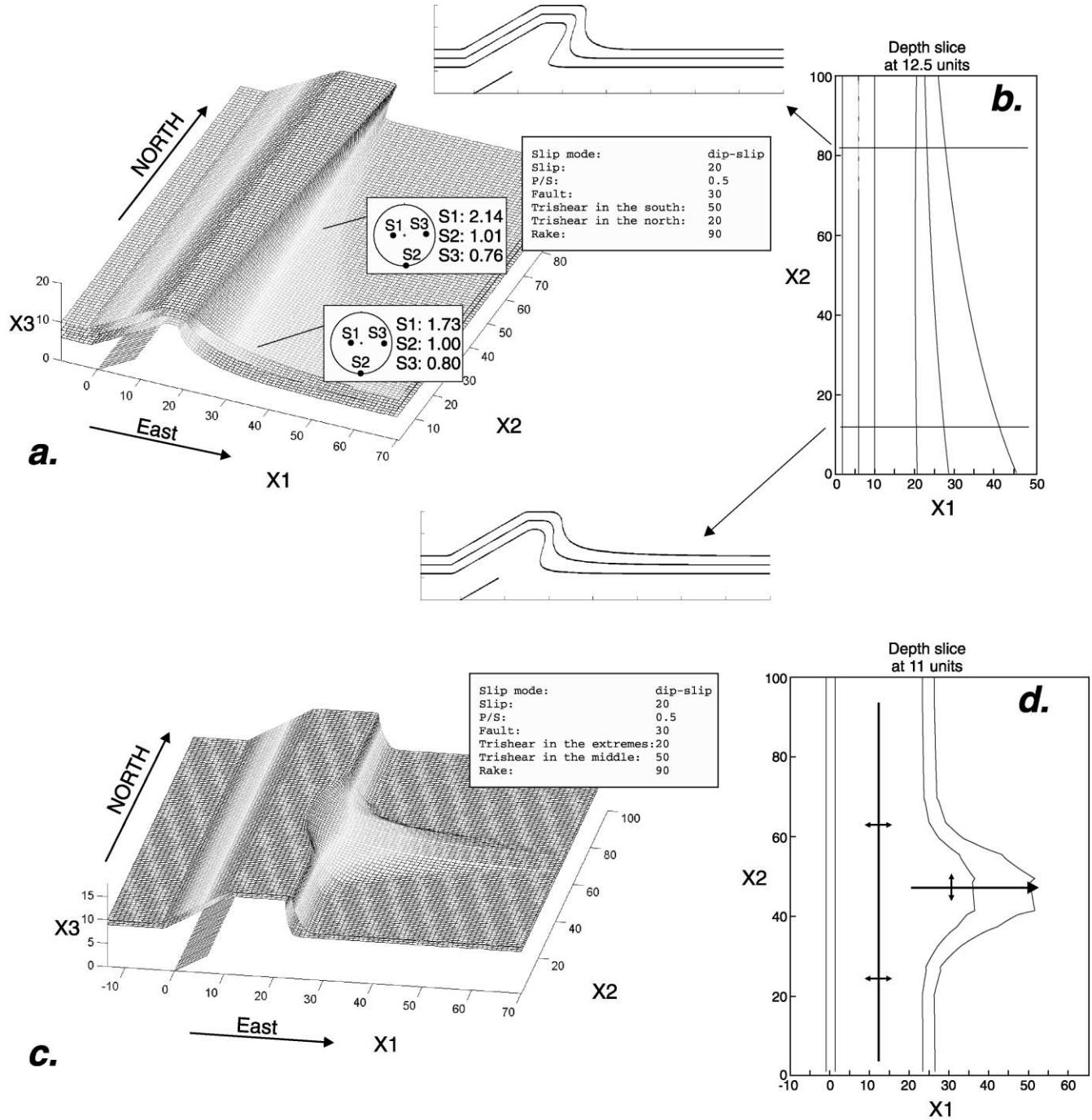

Fig. 5. Variation in trishear angle along strike. (a) Linear decrease in angle northward along strike produces an upright fold in the south but overturned to the north. The initial thickness of all the beds is the same. Two cross-sections through the model are shown. (b) Depth-slice of model in (a). Bed traces on forelimb diverge in direction of larger trishear angle. (c) Increase in trishear angle in the middle of the structure produces an anticline perpendicular to the trend of the main anticline. (d) Depth-slice of model in (c). Note that the backlimb remains unaffected by change in trishear angle on the forelimb.

significance of the trishear angle is unknown, this example must remain purely hypothetical.

4.4. Variable fault angle

A gradient in fault dip along strike produces changes in the dip of the forelimb, but in contrast to the previous examples, they also generate changes in the dip of the backlimb (Fig. 6a and b). As the fault dip diminishes, the trishear zone becomes sub-parallel to the strata and a very broad, low amplitude fold forms. Almost no rotations are recorded by the resulting strain ellipsoids (Fig. 6a).

A decrease of the fault angle in the middle of a structure results in more of the area in front of the main structure

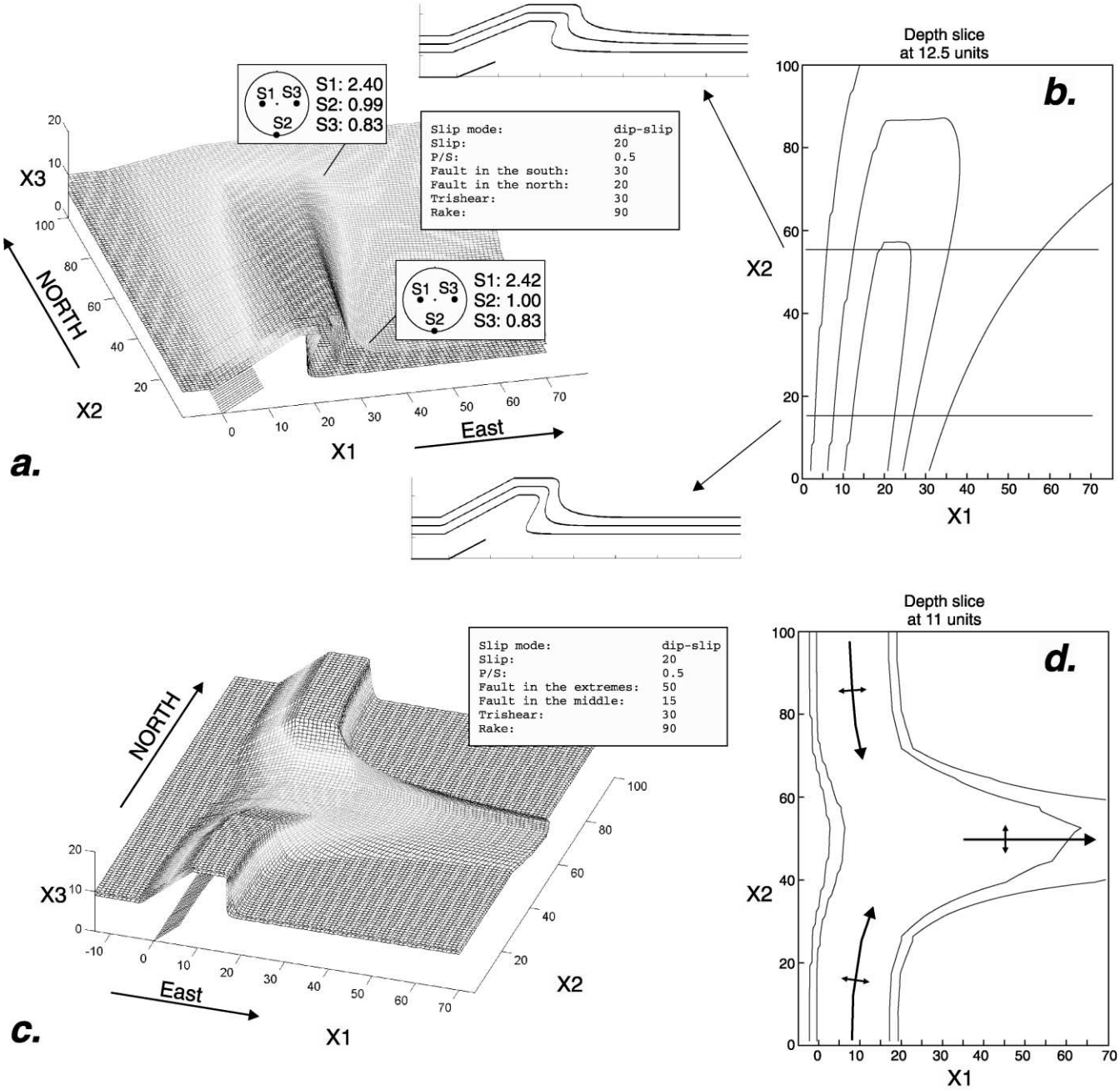

Fig. 6. Variation in fault dip along strike. (a) Linear decrease in dip from south to north. Strain values at two points on the forelimb shown with lower hemisphere projections. (b) Depth-slice of model in (a) highlighting the more gently dipping backlimb and a broad very gentle forelimb in the north. Two cross-sections through the model are shown. (c) Decrease in fault dip in the middle of the model also produces an anticline perpendicular to the main anticline. (d) Depth-slice of model in (c). The size of the orthogonal structure is larger than that in Fig. 5c because a decrease in the fault angle has the same effect on the forelimb as doubling the trishear apical angle. Note that the crest and backlimb are also affected.

becoming involved in the deformation. As in the above example of trishear apical angle gradient, an orthogonal fold appears in the front of the main structure (Fig. 6c and d). However, in this case, the entire crest and backlimb are also affected. The size of this orthogonal structure is bigger than in the previous example because a decrease of $\alpha°$ in the fault angle has the same effect in the forelimb as an increase of 2α in the trishear apical angle. The geometries shown here may resemble, at least superficially, certain fold interference patterns.

4.5. Oblique-slip

The geometries generated with oblique-slip (Fig. 7) are very similar to those generated by dip-slip. However, decreasing the rake (increasing the obliquity) has an effect

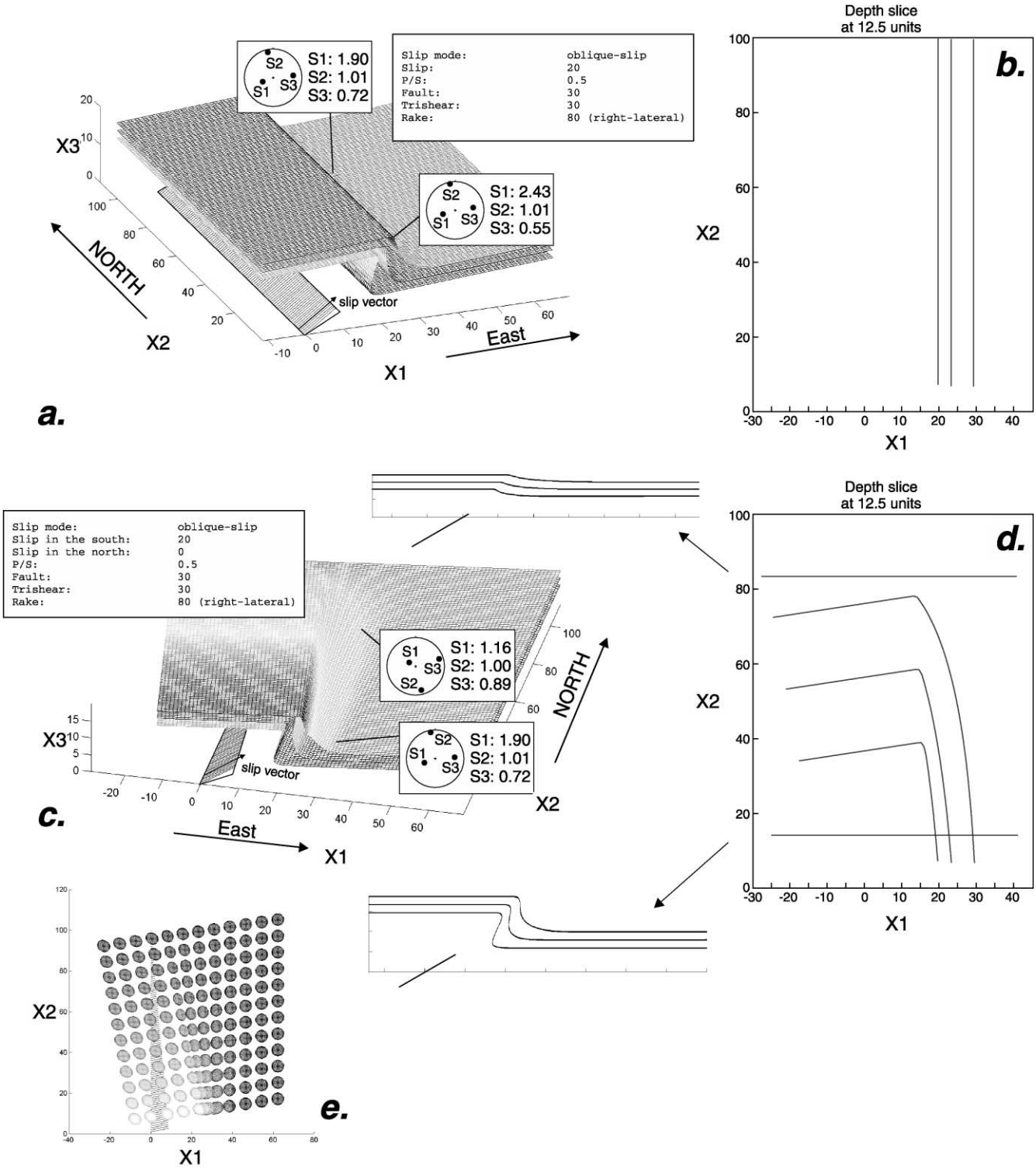

Fig. 7. Oblique slip deformation. (a) An example of oblique slip (rake = 80°) with all the variables constant along strike. The initial thickness of all the beds is the same. (b) Depth-slice of model in (a). The geometries generated with oblique-slip are very similar to those generated by dip-slip. However, decreasing the rake (increasing the obliquity) has a similar effect as decreasing the slip and increasing the trishear angle. (c) Same as (a) but with slip variation along strike. (d) Depth-slice of (c). Two cross-sections through the model are shown. The strain ellipsoid always has significant rotation in the horizontal plane, even where there is no variation along strike (a and b). This rotation is counter-clockwise in a right-lateral oblique-slip thrust and clockwise in left-lateral oblique-slip thrust. The rotation in (a) is about 10° counter-clockwise. Combining oblique-slip with a gradient in the trishear apical angle or in the slip along the strike, the rotation is increased if we sum the two effects (c and d, where rotation is ~15°), or minimized if we subtract them. (e) Map view of the projected ellipsoids of model of (c).

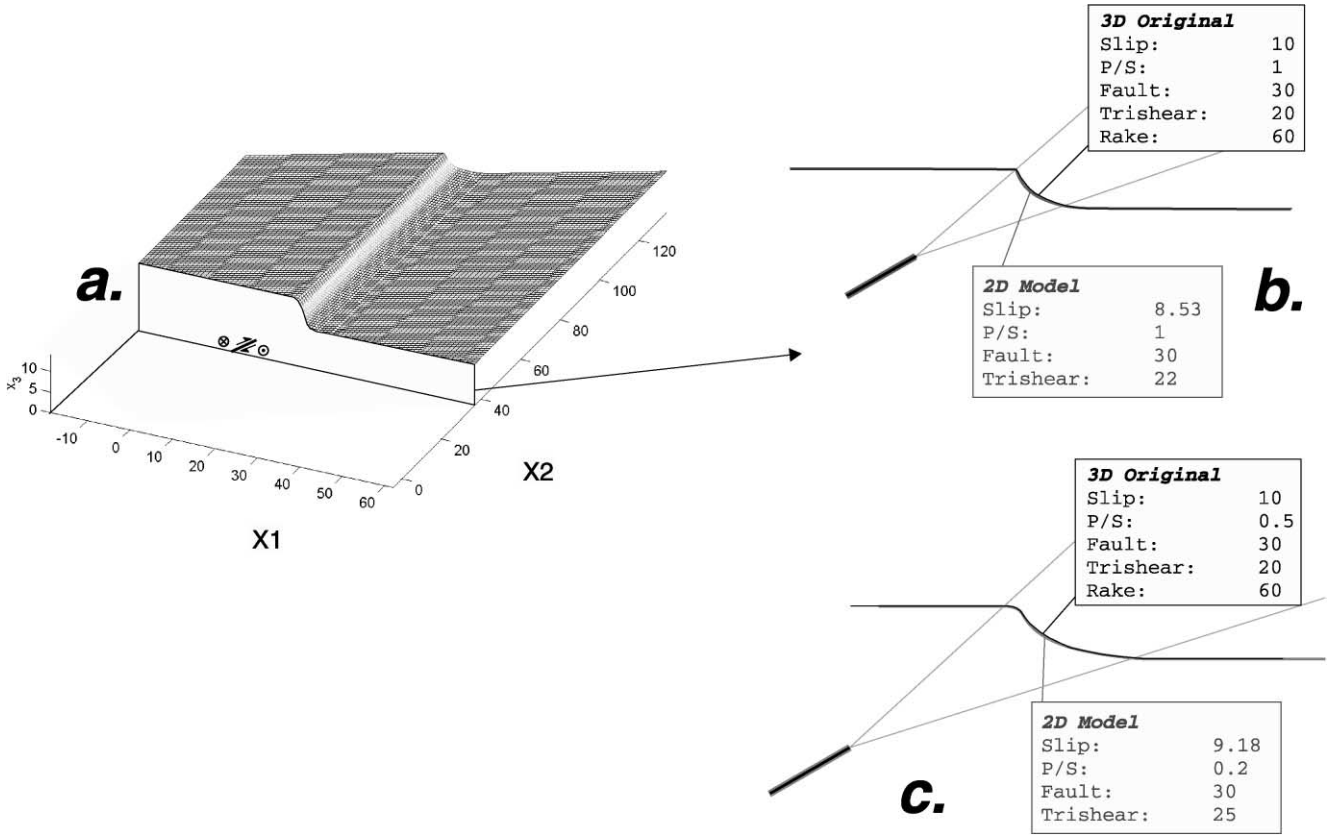

Fig. 8. Illustration of the errors that can occur if a trishear structure produced by oblique slip is assumed to have been produced by dip slip. (a) Oblique slip starting model. (b) Best fit 2D model determined using the grid search of Allmendinger (1998) superimposed on original 3D model. (c) Similar to (b) but with different starting parameters. In each case the main errors are in the estimation of the trishear angle, slip, and occasionally *P*/*S*.

similar to decreasing the slip and increasing the trishear angle. A 2D cross-section through a 3D oblique-slip structure could be modeled using the inverse grid search described by Allmendinger (1998) but the resulting model, though yielding excellent statistics, would be incorrect (Fig. 8). In the example of Fig. 8, the inverse method finds the correct *P*/*S* but overestimates the trishear angle and underestimates the slip.

The resulting strain ellipsoids for oblique-slip cases are clearly different than those of the previous examples. In analyzed examples, we see important rotation of principal axes in the horizontal plane, even in the simplest possible case where none of the model parameters varies along strike (Fig. 7a and b). The rotation is counter-clockwise in a right-lateral oblique-slip thrust and clockwise in left-lateral oblique-slip thrust. The ellipsoids from the model shown in Fig. 7a have rotated about 10° counter-clockwise. Oblique-slip can be combined with a gradient in the trishear apical angle or in the slip along the strike to produce large amounts of rotation if we sum the two effects, or minimize the rotation if we subtract them. For example, in Fig. 7c we have combined oblique-slip with a gradient in the slip along the strike, producing rotations of about 15°.

It is also important to note that, unlike pure dip-slip models, the intermediate strain axis is no longer horizontal. In examples where no parameters change along the strike, the intermediate axis is almost parallel to the pole to the movement plane (e.g. in Fig. 7a the S_2-axis dips 7° north). In more complex examples, it is more variable, as in Fig. 7c where it changes from 7° north (in the south) to 15° to the south (in the north). Because equivalent points of different sequential cross-sections are located in different parts of the trishear zone, they are controlled by different velocity fields. The resulting rotation produces an intermediate strain axis oblique to the pole of the movement plane. Comparing the map pattern of strain ellipsoids of Fig. 7e with the one of Fig. 3c (where only dip-slip is applied), we can see that in the dip-slip case (Fig. 3c) the axes of the ellipsoid projections tend to be parallel and orthogonal to the main structure but in the oblique-slip case (Fig. 7e) they tend to be oblique to it.

4.6. Growth strata

Growth strata can be modeled by adding new beds at different times during the evolution of the fault-fold system (Fig. 9a). By cutting the block in horizontal depth slices, we can visualize the map-view geometry of the growth strata. In Fig. 9, we show four examples in which the slip (Fig. 9a and b), *P*/*S* (Fig. 9c), trishear apical angle (Fig. 9d) and fault

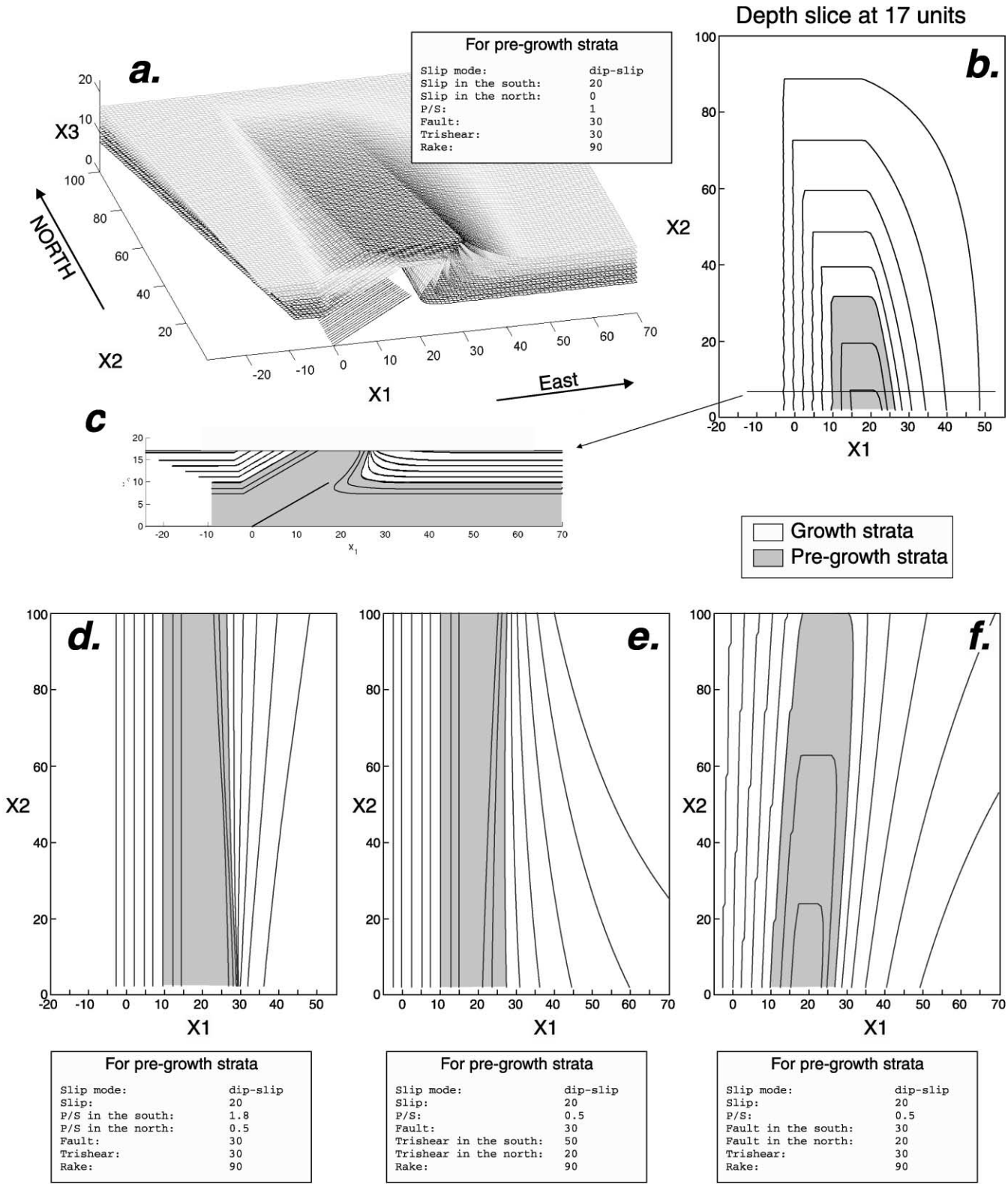

Fig. 9. Map view growth strata geometries. (a) Linear dip slip variation along strike. (b) Depth-slice of model in (a). (c) Representative cross-section of (b). (d–f) Depth-slices of examples where the slip, *P*/*S*, trishear apical angle and fault angle vary, respectively, along the strike as shown. In all the cases, the rate of sedimentation is greater than the uplift rate. The initial thickness of all the beds in a non-deformed region of the model is 1.25 units; the total maximum slip applied is 20 units (shortening of the pre-growth strata), and the sedimentation of the growth strata occurred at 3, 6, 9, 12 and 15 units of shortening.

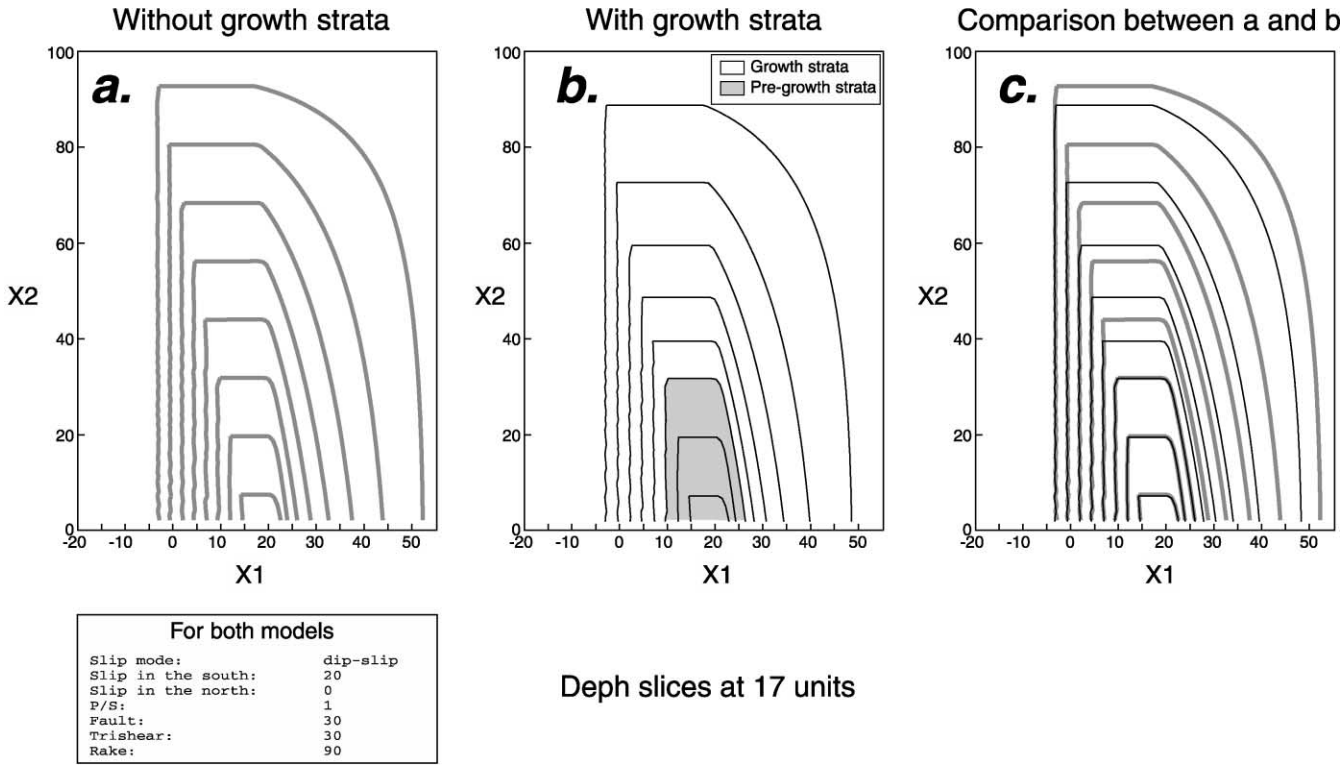

Fig. 10. Comparison of pre-growth with growth-strata geometries for a model with slip variation along strike. (a) Pre-growth only. (b) Same example as (a) but the last five beds were deposited during the deformation. (c) Superposition of (a) and (b), showing that the map patterns are very similar though not exactly the same. Nonetheless, it is very difficult to distinguish between growth and pre-growth strata from the map pattern.

angle (Fig. 9e) vary along the strike. In all the cases, the rate of sedimentation is higher than the uplift rate. The initial thickness of all the beds in an undeformed region of the model is 1.25 units; the total maximum slip applied is 20 units (shortening of the pre-growth strata), and the sedimentation of the growth strata occurred at 3, 6, 9, 12 and 15 units of shortening.

If we compare these map views with those without any growth strata (Figs. 4–6) we see that the map patterns are very similar, and that it is practically impossible to distinguish between growth and pre-growth strata using the map pattern. However, Fig. 10 shows that they are not exactly the same. Here we compare the map pattern of one model without growth strata (Fig. 10a) with another with the same initial conditions, but where the upper five beds are added during the deformation (Fig. 10b; is the same as Fig. 9). As we can see in this example, the growth-strata model is less elongated and narrower. A map pattern similar to the one of Fig. 10a can easily be confused with a growth-strata example. However, all of the beds in that example are pre-growth and of equal thickness prior to deformation.

5. Comparison with East Kaibab monocline

The East Kaibab structure, one of the typical monoclines of the Colorado Plateau of the western United States, is a NNE-trending, east-vergent basement-involved structure with an important deformation zone characterized by abundant and systematic faulting and fracturing (Davis, 1999; Tindall and Davis, 1999). Tindall and Davis (1999) have demonstrated that a significant clockwise strike-slip component acted together with a reverse dip-slip movement during Laramide formation of this structure. The monocline is relatively simple and the fault and fracture database that the authors present (Tindall and Davis, 1999) is very complete. Thus, we have chosen the East Kaibab monocline as a field test for the 3D-trishear model. Our intent is to evaluate the utility of the 3D-trishear model, not to produce a best fit to the real structure.

Tindall and Davis (1999) subdivided the structure into four domains (one to four from north to south, respectively). Domain number II (Fig. 11a), the simplest one, is characterized by synthetic NE-striking, NW-dipping faults with reverse and right-lateral offsets. Fig. 11b shows a cross-section along the line A–A′ in Fig.11a. In their interpretation, Tindall and Davis (1999) assume that the line of intersection of synthetic and antithetic faults is the intermediate stretch axis (S_2) and that the plane that contains the minimum and intermediate stretch axis (S_3–S_2) bisects the acute angle between the fault sets. Thus, for the entire structure they calculated the position of the three principal stretches of the finite strain ellipsoid as: $S_1 = 171°/41°$, $S_2 = 350°/48°$ and $S_3 = 261°/01°$ (Fig. 12a). Making the same assumptions,

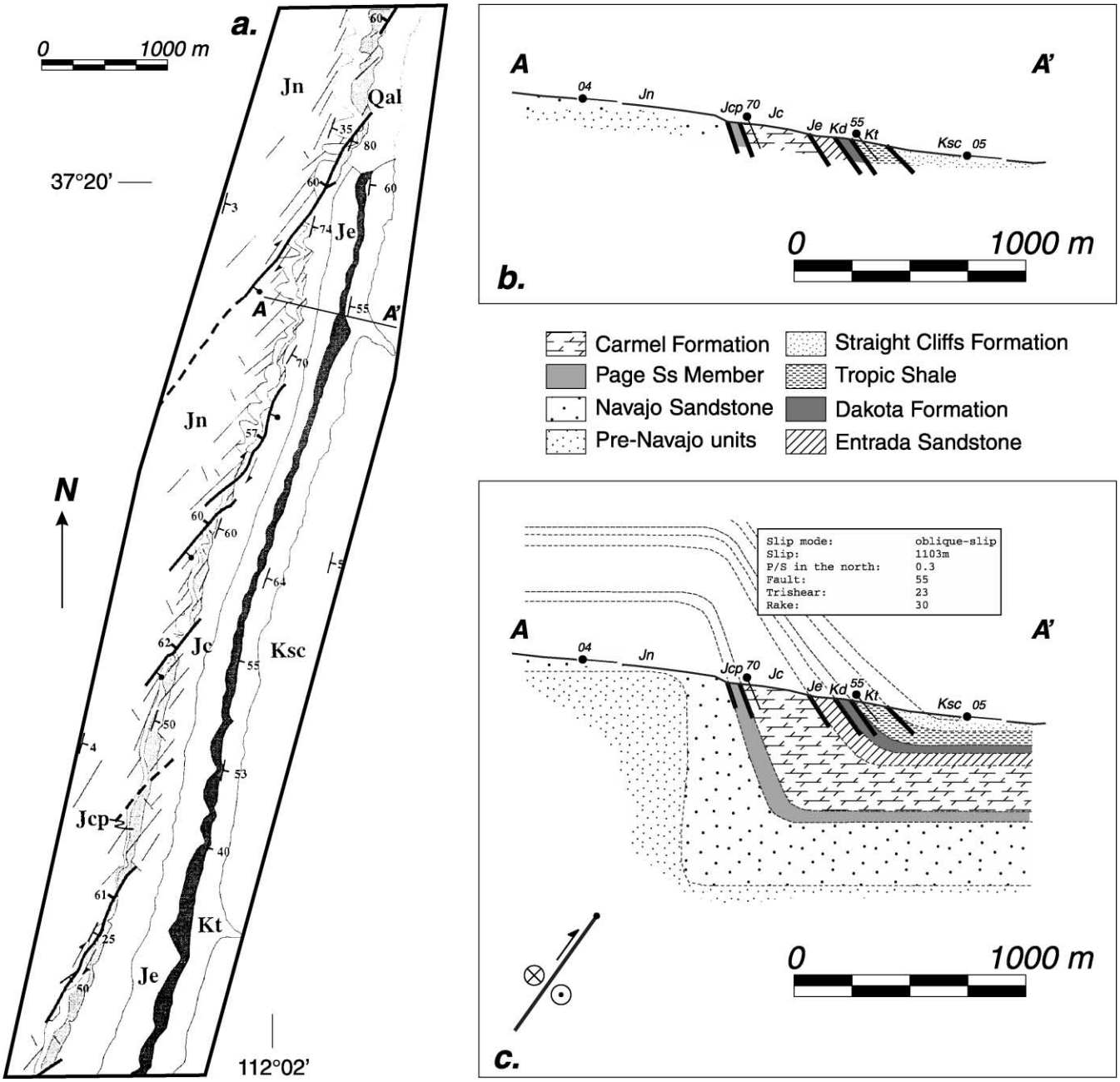

Fig. 11. (a) Geology of domain 2 of the East Kaibab Monocline in the Colorado Plateau, Utah, USA (from Tindall and Davis, 1999). (b) Cross-section along the line A–A′ where the outcropping units and the bedding plane dips are displayed. (c) 3D-trishear model consistent with the outcropping shape of the fold. Domain II shows a very regular behavior of the monocline along strike, and because of this, all the trishear variables are constant in the applied model. A rake of 30° from SW was used to model the field information. This is neither a unique nor a best-fit model, however, it is consistent with the geometry of domain II of the East Kaibab Monocline.

but based only on domain II data, the axes are: $S_1 = 146°/38°$, $S_2 = 309°/51°$ and $S_3 = 049°/08°$ (Fig. 12b and c). The typical rake of the slickenlines within the west-dipping faults of domain II is 30° from SW.

In Figs. 11c and 13a, we present a pseudo-3D trishear model that fits the exposed geometry of the fold. In domain II, the geometry of the monocline is very consistent along strike; thus in our model, all the trishear parameters are constant along strike. We used a rake of 30° from SW to be consistent with the field data. The unknown variables are the fault angle, trishear angle, *P*/*S*, slip and initial position of the tip line (place where the fault begins growing). Unfortunately, Allmendinger's (1998) grid search cannot be used to determine a statistical best fit for these variables because of the 3D nature of this problem and the massive computation it would entail. By trial and error, a reasonable approximation can be made, however: slip parallel to the slickenlines = 1103 m, $P/S = 0.3$, fault dip = 55°, trishear

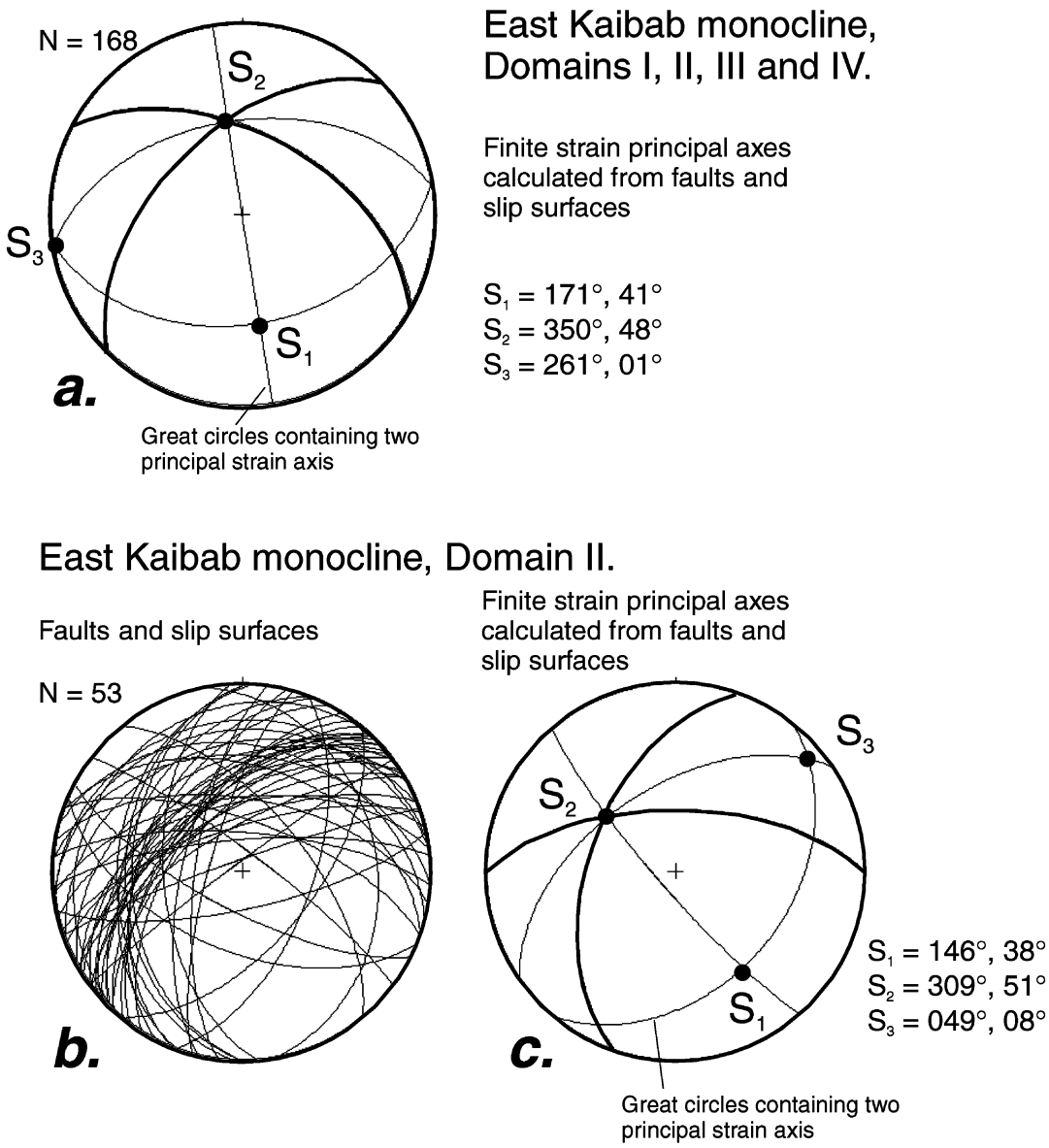

Fig. 12. (a) Principal strain axes interpreted by Tindall and Davis (1999), based on fault data from the East Kaibab Monocline. They assumed that the line of intersection of synthetic and antithetic faults is the intermediate stretch axes (S_2) and that the plane that contains the minimum and intermediate stretch axis (S_3–S_2) bisects the acute angle between the fault sets, (b) and (c) Using the same assumptions, but based only in domain II data, the axes are: $S_1 = 146°/38°$, $S_2 = 309°/51°$ and $S_3 = 049°/08°$.

angle = 23° and rake = 30° (see Fig. 11c for the final tip line position). This model is but one of the several possible alternatives that may explain the geometry of domain II of the East Kaibab monocline. The slip parallel to the slickenlines calculated by the model (1103 m) can be subdivided in 552 m of reverse dip-slip and 955 m of right-lateral strike-slip accommodated by a fault plane with azimuth 197° and dipping 55° to the west.

The strain recorded in the model yields an ellipsoid (Fig. 13b and c) with axes oriented: $S_1 = 183°/44°$, $S_2 = 332°/43°$ and $S_3 = 078°/15°$ that fits very well the field data of domain II (compare Figs. 12c and 13c). The relative lengths of the axes of the modeled ellipsoid are $S_1 = 1.53$, $S_2 = 0.99$ and $S_3 = 0.72$ (a length of one represents the radius of the initial sphere).

Tindall and Davis (1999) concluded that the final strain ellipsoid is more or less coaxial with the stress ellipsoid. Therefore, we use Reches' (1978) theory to calculate the fracture pattern consistent with the modeled strain (Fig. 13d). In this analysis, the four faults sets depend strongly on the ratio between the intermediate and maximum stretch axes ($k = S_2/S_1$). The result differs somewhat from that shown in Fig. 13c, which requires only two faults. However, if we compare the Reches (1978) prediction (Fig. 13d) with the field data for domain II (Fig. 12b) there are many similarities.

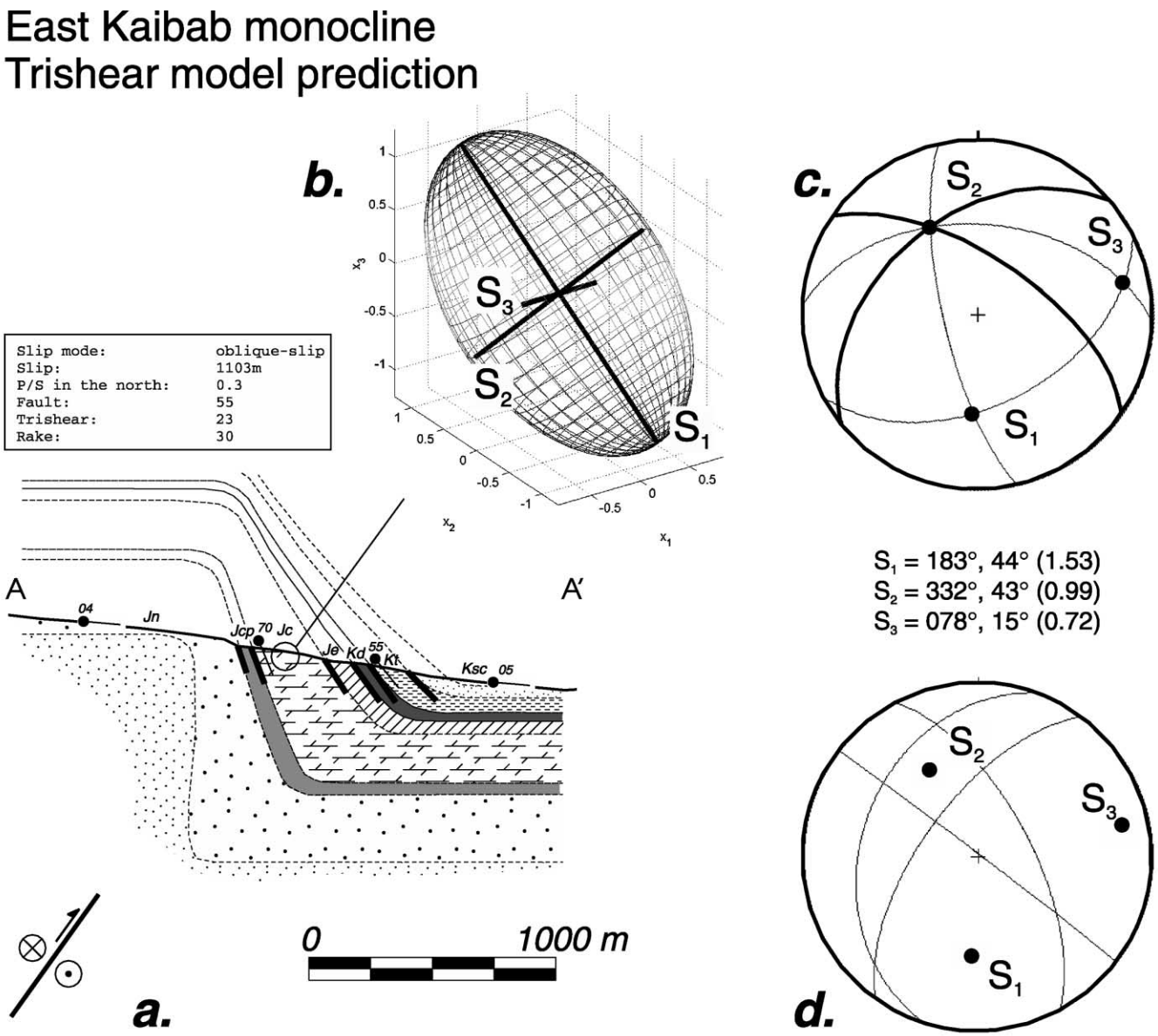

Fig. 13. (a) Possible 3D-trishear model that explains the outcropping shape of the domain II of the East Kaibab Monocline. (b) Forelimb strain extracted from the forward model in a 3D view and (c) plotted on a lower hemisphere equal area projection. S_1 is the greatest principal stretch and S_3 the least; the initial sphere had a radius of one. This plot also shows the fracture prediction of the model (heavy great circles) using the same assumptions as Tindall and Davis (1999); compare with Tindall and Davis' (1999) observed fractures in Fig. 12. (d) Fracture analysis following Reches (1978) using the principal strain axes predicted by the trishear model and assuming coaxial stress and strain. Compare this plot with Fig. 12b.

6. Conclusions

Different fold geometries can be derived by changing the variables of the trishear model along the strike of a structure. Because the number of possible combinations is infinite, many real structures could be modeled in this way. Some of the first order geometric conclusions are:

1. A thrust changing from blind to emergent can be explained either by changing the slip or *P*/*S* along strike. However, only the change in *P*/*S* produces cases where the fold axis does *not* plunge in the direction of the plunging fault tip line.
2. A fold where the forelimb changes from overturned to upright along strike can be explained either by changing the slip, the *P*/*S*, or the trishear angle along strike. The geometries resulting from these cases are substantially different and therefore their map patterns are also dissimilar.
3. A decrease in fault dip or an increase in trishear angle in the middle of the structure produces a fold oriented perpendicular to the trend of the main structure. The

geometry of this orthogonal structure can be easily confused with superposed structures.

4. Growth strata can be modeled by adding new beds at different times during the evolution of the fault-fold system. The geometries found are different from those constructed without growth strata. However, the models show that it is practically impossible to distinguish between growth and pre-growth strata using the map patterns.

Although it would be possible to write an algorithm to perform a 3D grid search analogous to that presented for the 2D case by Allmendinger (1998), current computing power makes this unfeasible. However, a trial and error manual fitting can be done if the 3D geometry of the real structure is sufficiently well defined by serial cross-sections, 3D-seismic time slices, 3D or 2D seismic-based isochron maps, well information, etc. In the field test presented here, a reasonable numerical model was obtained for the geometry and strain in the East Kaibab monocline (Davis, 1999; Davis et al., 1999; Tindall and Davis, 1999).

Acknowledgements

We are grateful to numerous colleagues for discussion of trishear fold kinematics. The reviews of the manuscript by Martha Withjack and Mark Fischer helped to improve the quality of the paper. This research was supported by grants from the Agencia Nacional de Promoción CientÍfica y Tecnológica (proyecto BID 802/OC-AR-PICT 00538) to Cristallini and National Science Foundation grant EAR-9814348 to Allmendinger.

References

Allmendinger, R.W., 1998. Inverse and fordward modeling of trishear fault-propagation folds. Tectonics 17 (4), 640–656.

Allmendinger, R.W., Zapata, T., Manceda, R., Dzelalija, F., 2001. Trishear kinematic modeling of structures with examples from the Neuquén Basin, Argentina. Thrust Tectonics Conference. American Association of Petroleum Geologists, Special Publication (in press).

Cooper, K., Hardy, S., 1999. The interaction between fault-related folding and sedimentation in 3D. Thrust Tectonics Conference, Royal Holloway, University of London. Abstract, p. 156.

Davis, G.H., 1999. Structural geology of the Colorado Plateau region of Southern Utah with special emphasis on deformation bands. Geological Society of America, Special Paper 342, 157pp.

Davis, G.H., Bump, A.P., GarcÍa, P.E., Ahlgren, S.G., 1999. Conjugate Riedel deformation band shear zones. Journal of Structural Geology 22, 169–190.

Erslev, E.A., 1991. Trishear fault-propagation folding. Geology 19, 617–620.

Erslev, E.A., Rogers, J.L., 1993. Basement-cover geometry of Laramide fault-propagation folds. In: Schmidt, C.J., Chase, R.B., Erslev, E.A. (Eds.). Laramide Basement Deformation in the Rocky Mountain Foreland of Western United States. Geological Society of America, pp. 125–146 Special Paper, 280.

Erslev, E.A., Mayborn, K.R., 1997. Multiple geometries and models of fault-propagation folding in the Canadian thrust belt. Journal of Structural Geology 19, 321–335.

Fischer, M.P., Wilkerson, M.S., 2000. Predicting the orientation of joints from fold shape: results of pseudo-three-dimensional modeling and curvature analysis. Geology 28 (1), 15–18.

Fischer, M.P., Wilkerson, M.S., Christensen, R.D., 1999. Three-dimensional evolution of trishear fault-propagation folds: relations between fold geometry, fault geometry and fault displacement (abs), Thrust Tectonics 99, Abstracts, Royal Holloway, University of London, p. 198.

Hardy, S., Ford, M., 1997. Numerical modeling of trishear fault propagation folding. Tectonics 16 (5), 841–854.

Jordan, T., Allmendinger, R., 1986. The Sierras Pampeanas of Argentina: a modern analogue of Laramide deformation. American Journal of Science 286, 737–764 New Haven.

Reches, Z., 1978. Analysis of faulting in three-dimensional strain field. Tectonophysics 47, 109–129.

Tindall, S.E., Davis, G.H., 1999. Monocline development by oblique-slip fault-propagation folding: the East Kaibab monocline, Colorado Plateau, Utah. Journal of Structural Geology 21, 1303–1320.

Zehnder, A.T., Allmendinger, R.W., 2000. Velocity field for the trishear model. Journal of Structural Geology 22, 1009–1014.